

Water-Mediated Conversion of BaTiO₃ Nanoparticles into BaCO₃ Nanorods in Electrospun Polymer Fibers: Implications for Carbon Capture Applications

Hasan Razouq, Kerstin Neuhauser, Gregor Zickler, Thomas Berger, and Oliver Diwald*



Cite This: ACS Appl. Nano Mater. 2023, 6, 19887–19895



Read Online

ACCESS |

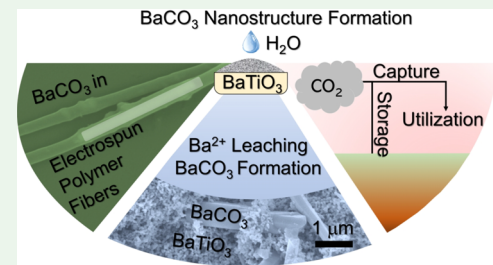
Metrics & More

Article Recommendations

Supporting Information

ABSTRACT: Under ambient conditions and in aqueous environments, transformations of nanoparticle-based ferroelectric components can raise important stability issues that are relevant for applications as multilayer capacitors, flexible piezoelectrics, or biomedical devices. We show that X-ray amorphous BaTiO₃ nanoparticles that were grown by flame spray pyrolysis and which can be incorporated into electrospun polymer fibers undergo incongruent Ba²⁺ dissolution in the presence of water. At pH > 5 and in contact with air, corresponding Ba solutes spontaneously convert into crystalline BaCO₃ needles to produce characteristic nano- and microstructures. We compared the reactivity of amorphous BaTiO₃ nanoparticle powders with those of nanocrystals after annealing-induced crystallization. The stability of aqueous nanoparticle–polymer formulations, which are typically part of nanoparticle encapsulation in polymers and electrospinning, was included in this analysis. Nanoparticle size, crystallinity, surface area, the presence of carbonaceous surface contaminants, and the effect of surface passivation with polymers are addressed to underline the critical role of condensed water during the synthesis, storage, and processing of BaTiO₃ nanoparticle-based composites.

KEYWORDS: BaTiO₃ nanoparticles, barium ion leaching, gas phase synthesis, nanoparticle carbonation, material processing, chemical weathering, electrospinning



INTRODUCTION

The stability of metal oxide nanostructures in aqueous environments is a key factor in the synthesis and processing of nanomaterials. Moreover, the understanding of the size-dependent stability of particle powders in contact with liquid water and/or CO₂ is very important for chemical weathering or aging of mineral binders.^{1–3} In particular, the reactivity of metal oxides of enhanced basicity, such as alkaline earth oxides, toward CO₂ has been addressed and the concomitant formation of carbonates with their characteristic crystal growth modes is of interest in the field of carbon capture and storage (CCS).⁴

BaCO₃ adopts characteristic crystal habits, such as rod-, whisker-, or needle-like crystal shape. There exists a wealth of information about BaCO₃ formation in aqueous environments. Great advances have been made about tuning the crystallite growth and morphology.^{5,6} The utilization of surface chemistry involving additives⁷ such as zwitterions, polymers, and/or polyelectrolytes has led to appropriate routes toward advanced mesocrystal architectures. Approaches for the generation of helical BaCO₃ mesocrystals^{8,9} that are built up from faceted and elongated BaCO₃ nanocrystals have been reported recently.

Perovskite BaTiO₃ nanoparticles, on the other hand, have gained substantial interest due to their ferroelectric properties

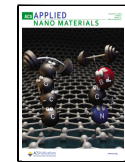
and the compound's high dielectric constant.^{10,11} Apart from their importance as source materials for the production of electroceramics, the size and scaling effects were studied as a result of the continuous miniaturization of electronic components, such as multilayer ceramic capacitors (MLCCs).¹² Polymer-based nanocomposite films that contain BaTiO₃ nanoparticles show favorable dielectric properties, while maintaining the transparency, flexibility, and workability of the polymer films.¹³ The acceptable biocompatibility of BaTiO₃ nanoparticles makes them promising candidates for biomedical applications and wearable bioelectronics.¹¹

The solid-state synthesis of BaTiO₃ (BTO) typically involves polycrystalline BaCO₃ and TiO₂ powders as educts.¹⁴ In the opposite direction, however, BTO can convert into BaCO₃¹⁵ in aqueous environment which is linked to technologically important processing routes of this compound.^{15–18} This topic is particularly relevant for the

Received: August 9, 2023

Accepted: October 2, 2023

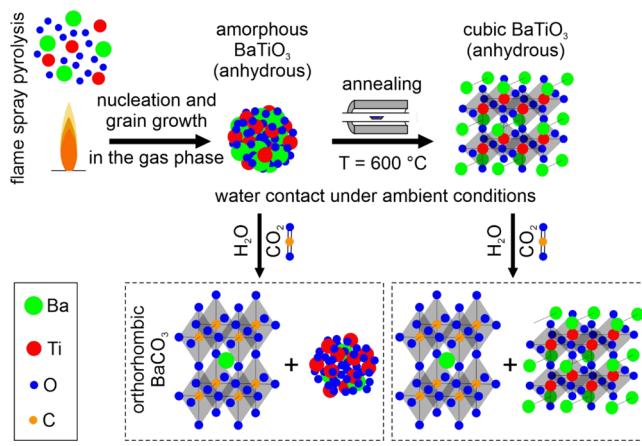
Published: October 19, 2023



utilization of submicrometer-sized BTO materials that need to be formulated for shaping of functional ceramics, such as the abovementioned MLCCs or piezoelectric devices. Manufacturing of such materials inherently involves colloidal processing in aqueous media, where related nanoparticle dispersions are cast, laminated, and sintered.

Here, we report on unexpected compositional and morphological transformations of gas-phase synthesized BTO nanoparticles in aqueous nanoparticle/poly(vinyl alcohol) dispersions upon colloidal processing and electrospinning. The fabrication of continuous fibers with diameters that can be scaled down to a few nanometers¹⁹ is particularly well-suited for the production of composite nanofibers incorporating metal oxide nanoparticles. These composite fibers give rise to significant specific surface areas of the material which hosts a rich network of particle–particle interfaces, enhancing their performance as sensors or catalyst components.²⁰ Poly(vinyl alcohol) (PVA), a widely used additive and polymer, offers several advantageous properties: it is highly hydrophilic, nontoxic, and biocompatible.²¹ Loaded with BTO nanoparticles, such ultrafine fibers can exploit the properties of the insulating, semiconducting,²² or piezoelectric properties that are used for flexible nanogenerators.²³ Motivated by the abovementioned unexplained materials transformations inside the polymer matrix, we carefully evaluated the process chain starting with amorphous BaTiO₃ nanoparticles and their interaction with water (**Scheme 1**) and succeeded in explaining the phenomena in terms of composition and structure of the particles (**Scheme 1**).

Scheme 1. Systematic Presentation of Experiments That Were Performed To Explain BaTiO₃ (BTO) Nanoparticle Stability during Processing and Electrospinning in Aqueous Poly(vinyl alcohol) (PVA) Formulations



This study is structured as follows: first, we report on the structural and compositional properties of electrospun nanoparticle/polymer fibers and address the water-mediated conversion of BTO nanoparticles into BaCO₃ rods in detail. Finally, we discuss the implications of these findings for colloidal processing of metal oxide nanomaterials for functional ceramics,^{10,12} BTO-polymer nanocomposites,^{13,24–26} or the potential of Ba²⁺ leaching for CO₂ adsorption.^{4,27}

EXPERIMENTAL METHODS

Particle Synthesis. We produced the barium titanate nanoparticle powder with a flame spray pyrolysis approach (FSP). The apparatus

used consists of a syringe pump, a burner, and a powder-collecting unit.^{28,29} The syringe pump (LA-160, HLL Landgraf) supplied the liquid fuel-precursor mixture at a constant flow rate of 2 mL/min. The precursor is transferred to the second unit (the burner) and sprayed through a nozzle. Oxygen dispersion gas (O₂ 5.0, dispersion gas) converts the precursor feed into fine droplets. The dispersion gas is supplied at volume flow of 3.0 L/min through a surrounding annular gap. The precursor fine droplets are ignited by a concentrically arranged methane and oxygen combustion flame (CH₄ 4.5, 1.5 L/min, O₂ 5.0, 2.0 L/min). Oxygen sheath flow (sheath gas, O₂ 5.0, 5.0 L/min) is guided through a sintered metal plate ring to ensure stoichiometric oxides production and to avoid byproducts. Mass flow controllers (Bronkhorst EL-FLOW) guarantee constant gas flow rates during the synthesis. A vacuum pump (Busch Seco SV 1040 C) ensures particle flow toward the particle collection unit. This unit consists of a glass fiber filter (Hahnemühle, GF6, Ø 257 mm) located on a water-cooled filter holder. Synthesis-related production parameters used for the synthesis of the here investigated nanoparticle powders are listed in **Table 1**.

Table 1. Process Parameters for BTO Synthesis via Flame Spray Pyrolysis³⁰

metal–organic precursor flow/mL min ⁻¹	2.0
dispersion gas (O ₂)/L min ⁻¹	3.0
supporting flame (CH ₄)/L min ⁻¹	1.5
supporting flame (O ₂)/L min ⁻¹	2.0
sheath gas (O ₂)/L min ⁻¹	5.0
pressure drop/bar	2–3

To prepare the precursor solution, the Ba precursor was dissolved under vigorous stirring at 120 °C for 3 h in 2-ethyl hexanoic acid. The liquid titanium precursor (titaniumisopropoxide, TTIP) is mixed with toluene and stirred for 3 h at room temperature before mixing with the dissolved Ba precursor.³⁰ Corresponding mixing ratios for a 100 mL batch are exemplified in **Table 2** and give rise to a Ti/Ba atomic ratio of 1:1.

Table 2. Precursor Parameters for the Synthesis of BTO via Flame Spray Pyrolysis^{30,31}

metal–organic precursor	amount (g)	dissolved in	amount (mL)
titanisopropoxide (TTIP) Sigma-Aldrich 97%	4.83	toluene Sigma-Aldrich 99,8%	50
bariumacetate (BaAc) EMSURE ACS p.a.	4.34	2-ethylhexansäure Sigma-Aldrich ≥99%	50

Annealing. After production, the BTO nanoparticle powder is transferred into fused silica cells, which allow thermal powder activation in alternating gas atmospheres of high vacuum ($p < 10^{-5}$ mbar) or O₂ atmosphere. Stepwise heating to 873 or 1173 K using a rate of 10 K min⁻¹ in a high vacuum ($p < 10^{-5}$ mbar) was performed to reduce surface contamination. After reaching the target temperature, the powder samples are exposed two times to molecular oxygen (20 mbar) for 30 min with a vacuum step for 30 min ($p < 10^{-5}$ mbar) in between.³⁰ This process removes carbon remnants arising from the metal–organic precursor by converting them into volatile CO and CO₂, which are removed upon continuous pumping. Fresh oxygen is added during cooling to room temperature to ensure carbon removal and to prohibit defect formation. Powders resulting from vacuum annealing to 873 or 1173 K are designated as the VA873 sample and VA1173 sample, respectively. Powders that were not subjected to any post-synthesis treatment are designated as-synthesized samples.

Electrospinning. Aqueous poly(vinyl alcohol) (PVA) (98.0–98.8% hydrolyzed M.W. 31,000–50,000) polymer solutions were used as a precursor for electrospinning, in which BTO nanoparticle powders were dispersed. Initially, a specific amount of polymer powder was dissolved in high-purity water (23 g/100 mL) under

continuous stirring at 90 °C for 3 h, resulting in a concentration of 23% w/v. Then, a specific amount of nanoparticle powder (60 mg/mL) was added to the polymer solutions under vigorous stirring. The dispersion was subjected to 30 min of stirring followed by 15 min of ultrasonic treatment. The materials were electrospun (Starter Kit Random, Linari Nanotech) by applying a potential of 18 kV, a pumping rate of 0.05 mL/h, and a 20 cm distance between the needle tip and the collector.

Electron Microscopy. Electron microscopy images were acquired by using scanning electron microscopy (SEM) and transmission electron microscopy (TEM). The SEM instrument (Zeiss FE-Ultra Plus 55) is equipped with a field-emission gun and Gemini lenses and was used at short working distances of around 3 mm and an accelerating voltage between 5–10 kV, with InLens and SE detectors. The TEM (JEOL JEM-F200 TEM) was operated at 200 kV and is equipped with a cold field emission electron source, a TVIPS F216 2k by 2k CMOS TEM camera, and a large windowless JEOL Centurio EDX detector. Particle size distribution plots before and after sintering and fiber diameters after thermal treatment were obtained from TEM images using the EM Measure software program from TVIPS. Selected area electron diffraction (SAED) images were recorded using a TVIPS F216 2k x 2k CMOS camera. The chemical composition of the samples is investigated by high-angle annular dark field (HAADF) images and energy-dispersive X-ray spectroscopy (EDX) maps.

X-ray Diffraction (XRD). X-ray diffraction data were collected at room temperature in coupled Theta–Theta mode on a Bruker D8 Advance diffractometer with a DaVinci design. The crystallite domain size was determined by applying the Scherrer equation to the main diffraction features.³² For quantitative phase analysis, the Rietveld method was applied by using the software TOPAS 4.2 (Bruker 2012). All X-ray diffraction measurements were performed on powder or ground samples to ensure a sufficient diffraction intensity that satisfies counting statistics. Electrospun fibers were frozen in liquid nitrogen for their solidification before being ground to form a powder.

Thermogravimetric Analysis. Thermogravimetric analyses were performed using an STA 449 F3 Jupiter instrument from Netzsch. The measurements were carried out in the range from room temperature to 1273 K and with a heating rate of 10 K/min under synthetic air. To perform the analysis, the nanoparticle powder was placed on an aluminum oxide crucible, which served as a sample holder.

Nitrogen Physisorption. Nitrogen physisorption was performed at 77 K (ASAP 2020 adsorption porosimeter, Micromeritics GmbH) and the specific surface area was calculated by applying the model of Brunauer–Emmet–Teller (BET). Prior to nitrogen sorption, the sample was degassed under a vacuum at 573 K for 3 h. The BET surface area was evaluated using adsorption data in a relative pressure range p/p_0 of 0.06–0.21.

Exposing the Powder to Condensed Water and in the Absence of Polymer. Approximately 50 mg of the nanoparticle powder was placed onto a Silicon wafer and then covered with a drop of deionized water (200 μ L). Right after, the resulting mixture was dried in air (for $t \leq 30$ min) at room temperature for further investigations. The samples investigated via SEM were dried at 80 °C to ensure complete water removal.

RESULTS AND DISCUSSION

The systematic evaluation of BTO nanoparticle powder reactivity toward liquid water was triggered by observations from polymer-encapsulated nanoparticles after their formulation with aqueous poly(vinyl alcohol) (PVA) mixtures for electrospinning (Figure 1).²⁰ If highly dispersed vapor phase grown metal oxide nanoparticles, such as those of TiO₂ or ZnO, show no reactivity toward water and the polymer, characteristic threads of particle chains can be isolated after annealing induced polymer removal.²⁰ The microstructural situation of as-synthesized BTO nanoparticle powders in water

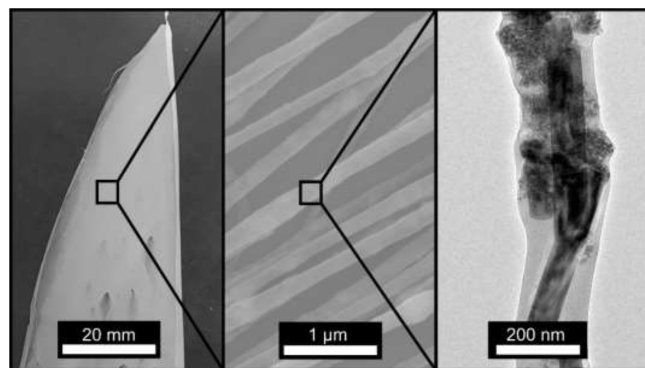


Figure 1. Digital photograph (left panel) and electron microscopy images—SEM image in the center and TEM image in the right panel—of electrospun PVA fibers from aqueous PVA formulations incorporating as-synthesized BTO nanoparticle powders.

formulated poly(vinyl alcohol) (PVA) dispersions, however, is very different (Figure 1).

At the length scale of micrometers (SEM image in the middle of Figure 1) the PVA-based fibers appear uniform, and the corresponding transmission electron microscopy (TEM) data (right panel of Figures 1 and S1) show encapsulated particles of high morphological definition which are much larger in size than the electrospun BTO nanoparticles forming agglomerates. Related rodlike features are elongated and clearly delimited by faceted interfaces. Apart from the fact that nanoparticle encapsulation inside electrospun fibers reveals important details about the organization of metal oxide particles inside the spatially confined organic matrices,³³ such a material integration approach is also advantageous for the in-depth structural analysis of individual particles by electron diffraction. In fact, selected area electron diffraction (SAED) measurements on such rods yield diffraction spots consistent with the BaCO₃ structure (Supporting Information, Figure S2).

TEM and XRD data reveal significant differences for electrospun fibers depending on the thermal pretreatment of the inorganic particles prior to polymer encapsulation. When the as-synthesized powder was used as a precursor for the electrospun fibers, the electron micrograph (Figure 2a) indicates the presence of larger rod-shaped particles, which, in addition to the as-synthesized particles, were frequently observed in such samples and attributed to BaCO₃. The diffraction pattern acquired on collected mats of such electrospun fibers (c) shows one PVA-specific reflection peak at $2\Theta = 19^\circ$ and a diffraction pattern that reveals BaCO₃ as the only crystalline phase present (Figure 2c). In contrast, the electron micrographs of electrospun PVA fibers loaded with VA873 nanoparticle powders (Figure 2b) show uniformly sized fibers that exclusively host small nanoparticle agglomerates. As shown recently, thermal annealing to $T \geq 873$ triggers the crystallization of amorphous BTO to convert into powders of BTO nanocrystals.³⁰ Following electrospinning, TEM analysis of many different sample regions did not reveal any evidence of BaCO₃ rods. In this case, XRD analysis confirms that the BTO nanoparticles adopt the tetragonal BTO phase and coexist with traces of crystalline BaCO₃ (see weak diffraction features marked with green triangles, bottom of Figure 2d). A quantitative phase analysis of the electrospun fibers loaded with BTO VA873 nanoparticle powders using Rietveld refinement indicates that only 4% of the total

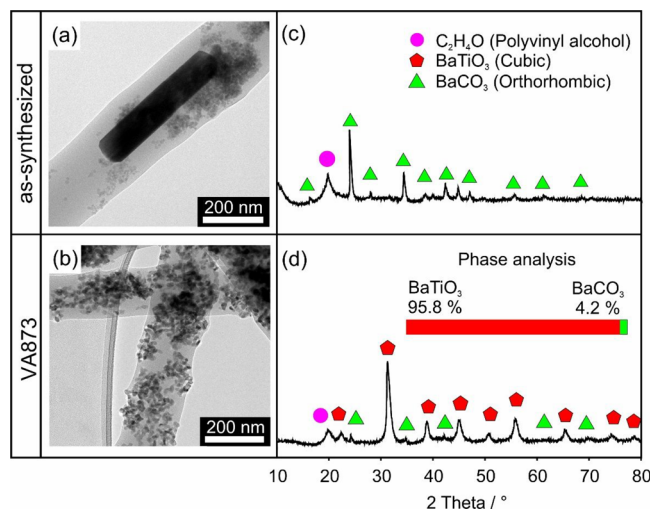


Figure 2. Characteristic TEM images (a, b) and XRD patterns (c, d) of electrospun fibers containing as-synthesized BTO nanoparticles (a, c) or BTO nanoparticles that were annealed to 873 K (VA873) prior to electrospinning (b, d). The inset in (d) highlights the abundance of the two crystalline phases, as determined by Rietveld refinement.

crystalline material adopts the orthorhombic BaCO₃ phase. Obviously, BTO VA873 exhibits enhanced stability toward BaCO₃ formation in the presence of PVA. A significantly higher fraction of ~ 14% of the total crystalline material was found to adopt the orthorhombic BaCO₃ phase in polymer free aqueous dispersions (see below). As pointed out in a previous study,³⁴ the dissolution properties of Ba²⁺ ions from BTO are significantly reduced by PVA in perfect agreement with our observations.

For the systematic analysis of the reactivity of FSP-derived nanoparticle powders toward water, we compared powder samples that were subjected to three different preannealing procedures. Specifically, samples of as-synthesized nanoparticle powders were vacuum-annealed to 873 K (BTO VA873) and 1173 K (BTO VA1173), respectively (Table 3).

XRD (Figure 3a–c) and thermogravimetric analysis (Figure 3d,e) as well as TEM analysis (including the particle size distribution functions derived from the TEM data Figure S3,

Table 3. Comparison of the Particle Size, Crystallite Domain Size, and BET-Specific Surface Area Values of As-Synthesized BTO Nanoparticle Powders and BTO Nanoparticle Powder Annealed to 873 and 1173 K

BTO sample type	average particle size [nm]	specific surface area [m ² ·g ⁻¹]	d _{XRD} [nm] Ref. ³⁰	particle crystallinity
as-synthesized	13	84 ± 12	-	-
BTO VA873	17	63 ± 9	12 ± 1	monocrystalline
BTO VA1173	73	21 ± 3	26 ± 7	polycrystalline

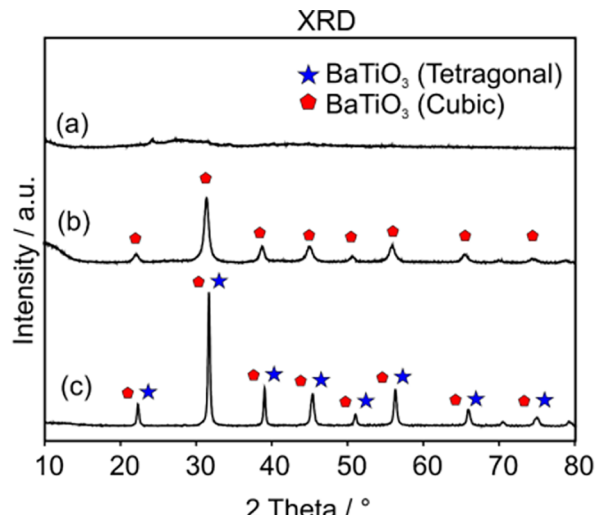


Figure 3. XRD patterns of as-synthesized BTO (a), BTO VA873 (b), and BTO VA1173 nanoparticle powders (c) and thermogravimetric analysis (TGA) results (d and e) obtained on as-synthesized BTO (d) and BTO VA873 nanoparticle powder (e) in synthetic air. Heating rate: 10 °C min⁻¹.

Supporting Information) provide (i) structural and morphological information about annealing-induced particle crystallization (Figure 3a–c), (ii) the decomposition and elimination of synthesis-related carbon and water residues (Figure 3d,e), and (iii) particle coarsening (Figure S3, Supporting Information).

The as-synthesized nanoparticle powder is X-ray amorphous with no crystalline diffraction features observed (Figure 3a, Table 3). The vacuum-annealed powder BTO VA873 shows diffraction features that are consistent with the cubic BTO phase (Table 3). Evaluation of the diffraction signal width points to an average crystallite domain size of 12 ± 1 nm. The XRD pattern of BTO VA1173 (Figure 3c) reveals the presence of the cubic and the tetragonal BTO phase. (Due to broadened diffraction features and based on XRD measurements alone, it is impossible to provide in this case a quantitative phase analysis.) Earlier Raman spectroscopy measurements on comparable materials^{30,35} in fact confirmed that both BTO phases, cubic and tetragonal BTO, are present in the BTO VA873 and BTO VA1173 samples. The crystallite domain size

was calculated to be around 26 ± 7 nm. Comparing this value with the average particle size (Table 3 and Figure S3f, Supporting Information) suggests that related particles are polycrystalline.³⁰

Driven by surface and interface minimization, particle coarsening is induced by annealing treatment at temperatures $T \leq 873$ K which triggers ion diffusion and mass transport in general. We expect that under the vacuum treatment applied here, particle coalescence contributes substantially to the growth of the grains.

As-synthesized nanoparticles are hydrated and contain synthesis-related carbon remnants. TGA of a pristine powder sample reveals that annealing to 873 K gives rise to a mass loss of about 17% (Figure 3d). Prior to their stability tests in water (as presented below), the application of 2–3 powder exposure cycles to oxygen (30 min each) with intermediate evacuation steps (continuous pumping to $p < 10^{-5}$ mbar for 30 min) is sufficient to effectively remove carbon from the BTO VA873 (Figure 3e) and BTO VA1173 powder samples.

We exposed as-synthesized as well as annealed powder samples to liquid water in air and at room temperature. Approximately 50 mg of the nanoparticle powder was deposited on a silicon wafer and covered with a drop of deionized water with an approximate volume of 200 μL . Drying in air and for a time interval not longer than 30 min leads to samples as characterized by SEM in Figure 4.

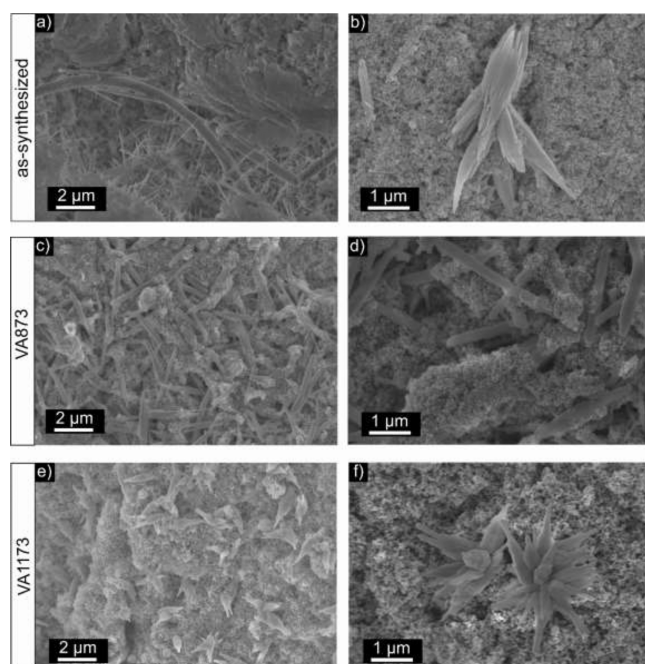


Figure 4. SEM images of as-synthesized BTO (a, b), BTO VA873 (c, d), and BTO VA1173 (e, f) nanoparticle powders after room temperature contact with liquid water and subsequent drying in air.

Exposure of as-synthesized BTO powder to water produces elongated structures, including needle-like, rod-shaped, and hairlike crystallites that grow out of aggregates of spherical nanoparticles (Figure 4a,b). The elongated structures show a wide range of sizes, between tens of nanometers to micrometers. Similar elongated structures were also observed in the VA873 powder sample after water contact (Figure 4c,d). In this case, the size distribution of the rods with lengths of a few micrometers and their morphology seem to be more

uniform and homogeneous, respectively. The SEM analysis of the VA1173 powder sample after water contact (Figure 4e,f) reveals clusters of roselike BaCO_3 structures that have formed at specific positions of the nanoparticle-based substrate. In terms of morphology, these structures are more uniform as compared to the as-synthesized powder after water contact.

After water contact of the as-synthesized amorphous BTO particle powder (Figure 5a), the diffraction pattern points to

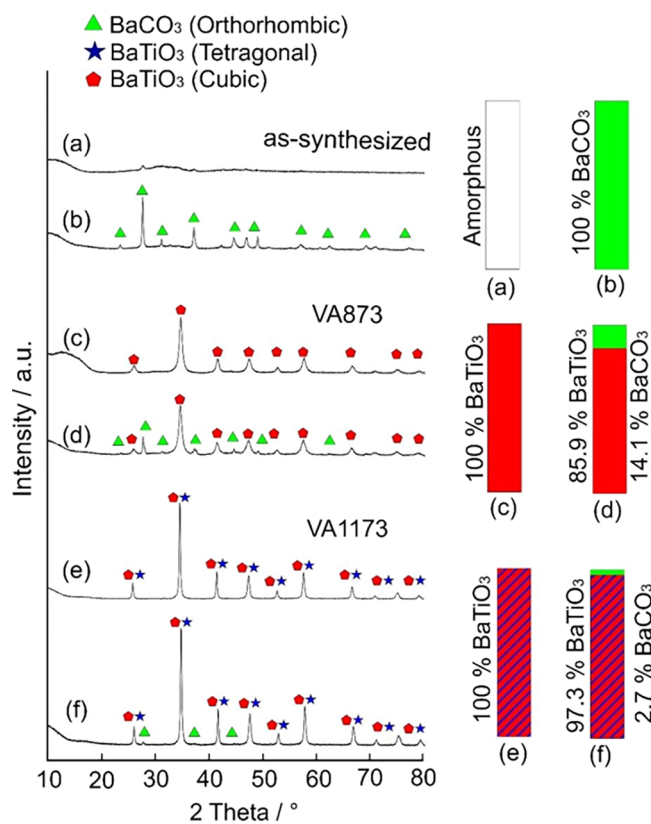


Figure 5. X-ray diffraction patterns and results from phase analysis of different BTO nanoparticle powders prior to (a, c, e) and after contact with liquid water (b, d, f). (a, b) As-synthesized powder, (c, d) BTO VA873 powder, and (e, f) BTO VA1173.

BaCO_3 as the exclusive crystalline phase (Figure 5b). BTO VA873 (Figure 5c) and VA1173 powder samples (Figure 5e), on the other hand, show BTO-specific diffraction patterns after contact with liquid water—additional features that originate from crystalline BaCO_3 (Figure 5d,f). Rietveld analysis indicates that approximately 14.1 or 2.7% of the VA873 and VA1173 samples convert into crystalline BaCO_3 , respectively. BTO nanoparticle exposure for 7 days to liquid water, both for as-synthesized and for BTO VA873 samples, does not change the materials conversion yield (Figure S4, Supporting Information). Densely packed rods and needles comprising flattened material surfaces (Figure S4a,b, Supporting Information) are observed for as-synthesized BTO. Related measurements on VA873 powders reveal the coexistence of both qualities, BaCO_3 rods and highly dispersed nanoparticle agglomerates (Figure S4c,d, Supporting Information). For this sample, Rietveld analysis did not reveal further changes in the crystallographic phase composition (Figure S4c,d, Supporting Information).

Finally, we analyzed the elemental distribution of Ba and Ti in as-synthesized and VA873 samples before and after water

treatment and acquired for this purpose energy-dispersive X-ray spectroscopy (EDX) maps (Figure 6, further details in Supporting Information, Figure S5).

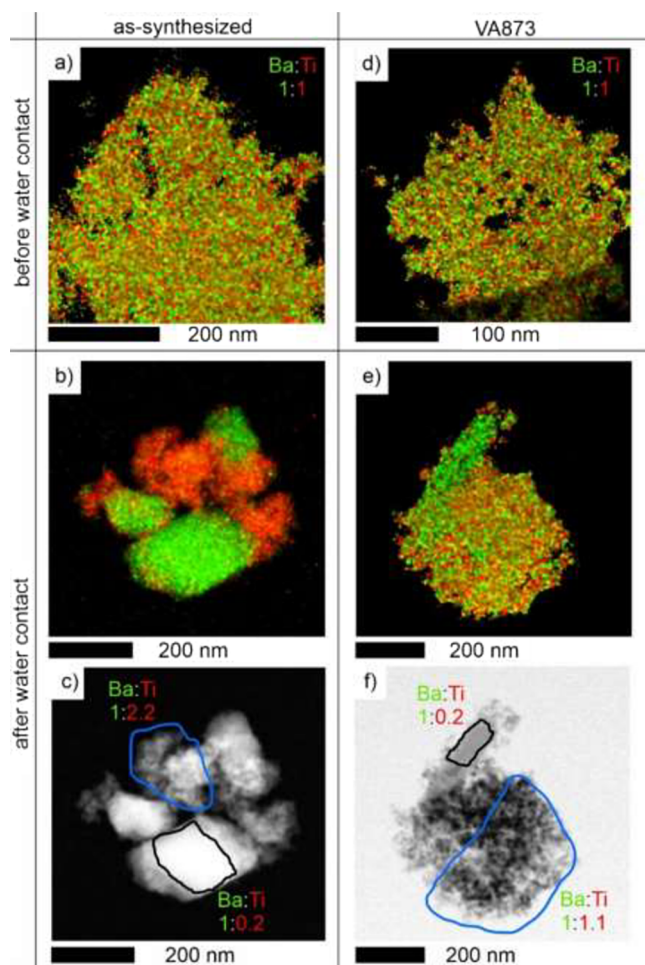


Figure 6. EDX quant maps acquired on as-synthesized BTO and BTO VA873 nanoparticle powders before (a, d) and after (b, e) contact with liquid water. Ba–Ti ratios of the as-synthesized and VA873 nanoparticle agglomerates before contact with water are highlighted in a and d, respectively. For water-treated samples, Ba–Ti ratios were determined for separate regions containing either predominantly nanoparticle aggregates (see blue-bordered region in c and f) or rods (black-bordered region in c and f).

Prior to water contact, as-synthesized BTO and BTO VA873 nanoparticle powders exhibit a homogeneous distribution of barium and titanium atoms, as shown by the EDX maps (Figure 6a,d). After data correction for software overshooting effects (see the Supporting Information for details), the Ba–Ti ratio was determined to be 1:1, which is consistent with ion concentrations of the precursor solutions and the respective flow adjusted for flame spray pyrolysis.^{30,31}

Significant separation into Ba-rich regions (hosting the micrometer-sized rods) or Ba-depleted regions (at adjacent nanoparticle regions) occurs upon sample exposure to liquid water (Figures 6 and S5). For the as-synthesized BTO as well as for the VA873 sample, regions featuring micrometer-sized rods (together with some nanoparticles in their vicinity) consistently yield an estimated Ba–Ti ratio of 1:0.2. This value corroborates the assignment of the rod-shaped structures to the BaCO₃ phase. (The non-negligible Ti signal detected for

these sample spots is attributed to the presence of some BTO nanoparticles in close contact with the rods' surface). Importantly, we found a significant difference in the elemental composition between as-synthesized BTO and the VA873 sample when analyzing the remaining nanoparticle fraction. In this case, Ba depletion is more pronounced for the as-synthesized sample (Ba–Ti = 1.0:2.2) as compared to the annealed sample (Ba–Ti = 1.0:1.1). The results corroborate the preferential Ba-leaching upon water contact from BTO nanoparticles. For the as-synthesized powders, ~55% of all Ba atoms are removed upon water exposure, whereas only ~9% of all Ba atoms are removed from a VA873 sample. The much stronger Ba depletion observed for the amorphous BTO powder points to barium dissolution both from the particles' surface and from bulk regions. On the other hand, we postulate that Ba leaching from VA873 and VA1173 crystalline powders is limited to the surface of the BTO nanoparticles. In line with such an interpretation, barium leaching is less extensive for VA1173 samples, featuring a lower surface area ($21 \pm 3 \text{ m}^2 \text{ g}^{-1}$) than the VA873 powder ($63 \pm 9 \text{ m}^2 \text{ g}^{-1}$), thus resulting in reduced carbonate formation. While the specific surface area of the two samples (before water exposure) differs by a factor of ~3, the BaCO₃ content (as determined by phase analysis after water treatment, Figure 6) differs even by a factor of ~5 (i.e., 14.1% for VA873 and 2.7% for VA1173, respectively). While these results corroborate the critical influence of the surface area on the degree of conversion, additional parameters seem to play a role.

From our observations, we deduce that at room temperature, highly dispersed BTO nanoparticle powders with specific surface areas of $60 \text{ m}^2 \text{ g}^{-1}$ and larger are unstable in aqueous environments and transform into crystalline BaCO₃ with characteristic crystal morphologies. The source of carbon is not perfectly clear since fractions of carbon may also originate from synthesis-related impurities as they exist on as-synthesized BTO nanoparticle powders (Figure 3e). Annealed and oxygen-treated BTO VA873 powder samples, however, are judged from thermogravimetric analysis, exempt from carbonaceous contaminants but do also convert into BaCO₃ upon reaction with CO₂ though to a less extent. Due to the complex interfacial materials situation related to the powder that is covered with condensed water, which in turn becomes continuously removed by drying in CO₂-containing air, it is impossible to decide for the here-reported experiments whether the CO₂ predominantly stems from the gas phase or serves in the form of dissolved species in liquid water as a precursor educt.

On average, crystalline BTO VA873 nanoparticles are slightly larger than amorphous as-synthesized particles. Values for the corresponding crystallite domain size ($12 \pm 1 \text{ nm}$) are consistent with the average particle size that was determined from TEM image analysis and particle counting ($d = 17 \text{ nm}$, Table 3).³⁵ The solid's crystallinity or its absence has a strong impact on the dissolution behavior. It is well-established that due to the generally larger enthalpy associated with the amorphous form, both the corresponding intrinsic dissolution rate and its solubility are generally larger for amorphous solids than those for their crystalline counterparts.³⁶ This is clearly reflected by the observations described in Figures 2, 4a–d, and 5. Amorphous BTO transforms into crystalline BaCO₃ to a significantly larger extent, whereas only a fraction of 14% of the crystalline BTO seems to convert into BaCO₃. (Figure 5c–d) Specific surface area values play an important role as well.

Powders of larger and polycrystalline BTO VA1173 particles with specific surface areas around $21 \text{ m}^2 \text{ g}^{-1}$, which corresponds to roughly a third of the BTO VA873 powder, remain essentially stable in condensed water (Figure 5e,f). Water contact leads to only 3% of the entire sample that is made up of BaCO_3 .

Apart from the general instability of anhydrous BTO nanoparticles in condensed water, it is also the enhanced kinetics of Ba extraction from the solid into the solution that represents a challenge in the liquid phase processing of BTO nanomaterials. This may be particularly relevant for the production of BTO-based electroceramics, which involves sintering as the key process step after shaping the workable mass (powder or an aqueous paste). Our literature research revealed that there exist several reports about abnormal grain growth of BTO nanomaterials after processing and sintering at temperatures $T > 1100 \text{ }^\circ\text{C}$.^{37–39} One study even described abnormal grain growth even within electrospun fibers, where water was also inevitably involved in the preceding materials processing. The authors clearly indicate that an intermediate BaCO_3 phase has formed, which is also consistent with independent report,⁴⁰ but decomposes at temperatures above $700 \text{ }^\circ\text{C}$. In complex metal oxides and perovskites such as BTO, abnormal grain growth is a common phenomenon and can have multiple reasons.^{41,42} One obvious reason that is associated with the use of nanomaterials, however, would be that during the overall process large-grained BaCO_3 structures of the type described in Figures 1 and 2a have formed as intermediates to serve as precursor grain for the significantly larger BTO grains that result from subsequent sintering-induced carbonate decomposition. Inspection of the electron microscopy data reported in refs 39 and 40 with structures reported in this study may substantiate this hypothesis, which is also in line with the earlier reported effects of residual BaCO_3 on the dedensification of BTO during sintering.⁴³

CONCLUSIONS

If BaTiO_3 nanoparticle powders are grown in the gas phase, i.e., under anhydrous conditions and in the absence of organic solvents, they exhibit enhanced reactivity toward liquid water. In many cases, however, water cannot be excluded from subsequent materials processing steps for economic and environmental reasons. This work reveals the role of size and crystallinity of highly dispersed BaTiO_3 particle systems, which represent a prototypical nanomaterial component within ferro- and piezoelectric devices. Pronounced crystallinity and/or contact with hydroxyl-containing polymers such as poly(vinyl alcohol) (PVA) stabilizes the material against incongruent Ba^{2+} dissolution, Ba^{2+} leaching and BaCO_3 formation. The thermodynamic instability of BTO in water and resulting deviations from the desired stoichiometry enables exaggerated grain growth and explains the sometimes observed evolution of inhomogeneous microstructures.^{17,18,44}

From another perspective, it should be emphasized that the spontaneous evolution of micrometer-sized and crystalline objects such as the BaCO_3 fibers, needles, and whiskers occurs wherever condensed water and gaseous CO_2 come in simultaneous contact with dissolved and locally released Barium ions. In nature, cycles of carbonate dissolution and crystallization strongly impact the CO_2 balance in the earth's atmosphere. In particular, the reactivity of Ba^{2+} containing multinary metal oxides, e.g., in the form of waste multilayer ceramic capacitors (MLCCs), and the concomitant formation

of carbonates with their characteristic crystal growth modes may be relevant for carbon capture and storage (CCS).⁴ CO_2 binding capacity and carbonate formation of Ba^{2+} seem to be comparable to those of Ca^{2+} . Control over the size of the metal carbonate particles is a key point for optimization of this CCS approach and involves parameters such as the release of Ba^{2+} ions and their local concentration in solution. This opens an opportunity window for carbon capture in combination with the spatially controlled deposition of carbonate structures at natural and engineered surfaces and pore structures.

ASSOCIATED CONTENT

Supporting Information

The Supporting Information is available free of charge at <https://pubs.acs.org/doi/10.1021/acsanm.3c03703>.

Additional transmission electron microscopy data and electron diffraction data of electrospun metal oxide and carbonate particles and EDX quant maps showing the elemental distribution of Ba and Ti ions ([PDF](#))

AUTHOR INFORMATION

Corresponding Author

Oliver Diwald – Department of Chemistry and Physics of Materials, Paris-Lodron University Salzburg, A-5020 Salzburg, Austria;  orcid.org/0000-0002-2425-5281; Email: oliver.diwald@plus.ac.at

Authors

Hasan Razouq – Department of Chemistry and Physics of Materials, Paris-Lodron University Salzburg, A-5020 Salzburg, Austria

Kerstin Neuhauser – Department of Chemistry and Physics of Materials, Paris-Lodron University Salzburg, A-5020 Salzburg, Austria

Gregor Zickler – Department of Chemistry and Physics of Materials, Paris-Lodron University Salzburg, A-5020 Salzburg, Austria

Thomas Berger – Department of Chemistry and Physics of Materials, Paris-Lodron University Salzburg, A-5020 Salzburg, Austria;  orcid.org/0000-0002-2062-5193

Complete contact information is available at:
<https://pubs.acs.org/10.1021/acsanm.3c03703>

Author Contributions

The manuscript was written through contributions of all authors. All authors have given approval to the final version of the manuscript.

Funding

Open Access is funded by the Austrian Science Fund (FWF).

Notes

The authors declare no competing financial interest.

ACKNOWLEDGMENTS

The authors gratefully acknowledge support from the Austrian Science Fund FWF for project no. P34906 (Charge Separation in Metal Oxide Nanocomposites) and the financial support of the Salzburg Center for Smart Materials (P1727558-IWB01), which in turn is funded by the EFRE (European Funds for Regional Development) as well as AWS (Austrian Wirtschafts Service).

■ REFERENCES

- (1) Diwald, O.; Berger, T. *Metal Oxide Nanoparticles, 2 Volume Set: Formation, Functional Properties, and Interfaces*; John Wiley & Sons Incorporated, 2022, DOI: 10.1002/9781119436782.
- (2) Bañuelos, J. L.; Borguet, E.; Brown, G. E.; Cygan, R. T.; DeYoreo, J. J.; Dove, P. M.; Gaigeot, M.-P.; Geiger, F. M.; Gibbs, J. M.; Grassian, V. H.; Ilgen, A. G.; Jun, Y.-S.; Kabengi, N.; Katz, L.; Kubicki, J. D.; Lützenkirchen, J.; Putnis, C. V.; Remsing, R. C.; Rosso, K. M.; Rother, G.; Sulpizi, M.; Villalobos, M.; Zhang, H. Oxide- and Silicate-Water Interfaces and Their Roles in Technology and the Environment. *Chem. Rev.* 2023, 123, 6413 DOI: 10.1021/acs.chemrev.2c00130.
- (3) Baumann, S. O.; Schneider, J.; Sternig, A.; Thomele, D.; Stankic, S.; Berger, T.; Grönbeck, H.; Diwald, O. Size Effects in MgO Cube Dissolution. *Langmuir* 2015, 31 (9), 2770–2776.
- (4) Fu, L.; Ren, Z.; Si, W.; Ma, Q.; Huang, W.; Liao, K.; Huang, Z.; Wang, Y.; Li, J.; Xu, P. Research Progress on CO₂ Capture and Utilization Technology. *J. CO₂ Util.* 2022, 66, No. 102260.
- (5) Jiao, J.; Liu, X.; Gao, W.; Wang, C.; Feng, H.; Zhao, X.; Chen, L. Two-Step Synthesis of Witherite and Tuning of Morphology. *Mater. Res. Bull.* 2010, 45 (2), 181–185.
- (6) Zhang, Y.; Xie, B.; Zhang, R. Morphology Control of BaCO₃ by Template and Polymer-Inorganic Precursor. *New J. Chem.* 2018, 42 (3), 1585–1589.
- (7) Grimes, R. T.; Bennett, J. W. Surface Transformation Thermodynamics of Alkaline Earth Carbonates using First-Principles Calculations. *Surf. Sci.* 2022, 726, No. 122165.
- (8) Yu, S.-H.; Cölfen, H.; Tauer, K.; Antonietti, M. Tectonic Arrangement of BaCO₃ Nanocrystals into Helices induced by a Racemic Block Copolymer. *Nat. Mater.* 2005, 4 (1), 51–55.
- (9) Sturm Née Rosseeva, E. V.; Cölfen, H. Mesocrystals: Structural and Morphogenetic Aspects. *Chem. Soc. Rev.* 2016, 45 (21), 5821–5833.
- (10) Buscaglia, V.; Randall, C. A. Size and Scaling Effects in Barium Titanate. An Overview. *J. Eur. Ceram. Soc.* 2020, 40 (11), 3744–3758.
- (11) Sood, A.; Desseigne, M.; Dev, A.; Maurizi, L.; Kumar, A.; Millot, N.; Han, S. S. A Comprehensive Review on Barium Titanate Nanoparticles as a Persuasive Piezoelectric Material for Biomedical Applications: Prospects and Challenges. *Small* 2023, 19 (12), No. e2206401.
- (12) Hong, K.; Lee, T. H.; Suh, J. M.; Yoon, S.-H.; Jang, H. W. Perspectives and Challenges in Multilayer Ceramic Capacitors for Next Generation Electronics. *J. Mater. Chem. C* 2019, 7 (32), 9782–9802.
- (13) Suematsu, K.; Arimura, M.; Uchiyama, N.; Saita, S. Transparent BaTiO₃ /PMMA Nanocomposite Films for Display Technologies: Facile Surface Modification Approach for BaTiO₃ Nanoparticles. *ACS Appl. Nano Mater.* 2018, 1 (5), 2430–2437.
- (14) Buscaglia, M. T.; Bassoli, M.; Buscaglia, V.; Alessio, R. Solid-State Synthesis of Ultrafine BaTiO₃ Powders from Nanocrystalline BaCO₃ and TiO₂. *J. Am. Ceram. Soc.* 2005, 88 (9), 2374–2379.
- (15) Usher, T.-M.; Kavey, B.; Caruntu, G.; Page, K. Effect of BaCO₃ Impurities on the Structure of BaTiO₃ Nanocrystals: Implications for Multilayer Ceramic Capacitors. *ACS Appl. Nano Mater.* 2020, 3 (10), 9715–9723.
- (16) Yoon, D.-H.; Lee, B. I.; Badheka, P.; Wang, X. Barium Ion Leaching from Barium Titanate Powder in Water. *J. Mater. Sci: Mater. Electron.* 2003, 14 (3), 165–169.
- (17) Neubrand, A.; Lindner, R.; Hoffmann, P. Room-Temperature Solubility Behavior of Barium Titanate in Aqueous Media. *J. Am. Ceram. Soc.* 2000, 83 (4), 860–864.
- (18) Olhero, S. M.; Kaushal, A.; Ferreira, J. M. Preventing Hydrolysis of BaTiO₃ Powders during Aqueous Processing and of Bulk Ceramics after Sintering. *J. Eur. Ceram. Soc.* 2015, 35 (9), 2471–2478.
- (19) Tan, S.-H.; Inai, R.; Kotaki, M.; Ramakrishna, S. Systematic Parameter Study for ultra-fine Fiber Fabrication via Electrospinning Process. *Polym. J.* 2005, 46 (16), 6128–6134.
- (20) Razouq, H.; Berger, T.; Hüsing, N.; Diwald, O. Vapor Phase-Grown TiO₂ and ZnO Nanoparticles Inside Electrospun Polymer Fibers and their Calcination-induced Organization. *Monatsh. Chem.* 2023, 7, 11108.
- (21) DeMerlis, C. C.; Schoneker, D. R. Review of the Oral Toxicity of Polyvinyl Alcohol (PVA). *Food Chem. Toxicol.* 2003, 41 (3), 319–326.
- (22) Park, J.-C.; Ito, T.; Kim, K.-O.; Kim, K.-W.; Kim, B.-S.; Khil, M.-S.; Kim, H.-Y.; Kim, I.-S. Electrospun Poly(Vinyl Alcohol) Nanofibers: Effects of Degree of Hydrolysis and Enhanced Water Stability. *Polym. J.* 2010, 42 (3), 273–276.
- (23) Zhao, B.; Chen, Z.; Cheng, Z.; Wang, S.; Yu, T.; Yang, W.; Li, Y. Piezoelectric Nanogenerators Based on Electrospun PVDF-Coated Mats Composed of Multilayer Polymer-Coated BaTiO₃ Nanowires. *ACS Appl. Nano Mater.* 2022, 5 (6), 8417–8428.
- (24) Chen, R.-C.; Zhang, Q.-P.; Ke, K.; Sun, N.; Xu, W.-D.; Liu, D.-L.; Yang, W.; Li, Y.-T.; Zhou, Y.-L.; Yang, M.-B.; Yuan, J.; Yang, W. Chemically Bonding BaTiO₃ Nanoparticles in Highly Filled Polymer Nanocomposites for Greatly Enhanced Dielectric Properties. *J. Mater. Chem. C* 2020, 8 (26), 8786–8795.
- (25) Jia, Y.; Yang, C.; Chen, X.; Xue, W.; Hutchins-Crawford, H. J.; Yu, Q.; Topham, P. D.; Wang, L. A Review on Electrospun Magnetic Nanomaterials: Methods, Properties and Applications. *J. Mater. Chem. C* 2021, 9 (29), 9042–9082.
- (26) Starr, J. D.; Andrew, J. S. Janus-Type Bi-Phasic Functional Nanofibers. *Chem. Commun.* 2013, 49 (39), 4151–4153.
- (27) Wang, J.; Fu, R.; Wen, S.; Ning, P.; Helal, M. H.; Salem, M. A.; Xu, B. B.; El-Bahy, Z. M.; Huang, M.; Guo, Z.; Huang, L.; Wang, Q. Progress and Current Challenges for CO₂ Capture Materials from Ambient Air. *Adv. Compos. Hybrid Mater.* 2022, 5 (4), 2721–2759.
- (28) Mädler, L.; Kammler, H. K.; Mueller, R.; Pratsinis, S. E. Controlled Synthesis of Nanostructured Particles by Flame Spray Pyrolysis. *J. Aerosol Sci.* 2002, 33 (2), 369–389.
- (29) Niedermann, M.; Schwab, T.; Diwald, O. Nanoparticle Synthesis in the Gas Phase. In *Metal Oxide Nanoparticles*; Diwald, O., Berger, T., Eds.; Wiley, 2021; pp. 67–108.
- (30) Neige, E.; Diwald, O. Paramagnetic Electron Centers in BaTiO₃ Nanoparticle Powders. *Phys. Chem. Chem. Phys.* 2021, 23 (22), 12881–12888.
- (31) Schädli, G. N.; Büchel, R.; Pratsinis, S. E. Nanogenerator Power Output: Influence of Particle Size and Crystallinity of BaTiO₃. *Nanotechnology* 2017, 28 (27), 275705.
- (32) Weidenthaler, C. Pitfalls in the Characterization of Nanoporous and Nanosized Materials. *Nanoscale* 2011, 3 (3), 792–810.
- (33) Razouq, H.; Zickler, G. A.; Berger, T.; Hüsing, N.; Diwald, O. Topotactic Metal Hydroxide Decomposition to Organize Metal Oxide Nanoparticles Inside Electrospun Fibers. *Ceram. Int.* 2023, 49 (6), 10172–10175.
- (34) Paik, U.; Hackley, V. A.; Lee, J.; Lee, S. Effect of Poly(Acrylic Acid) and Poly(Vinyl Alcohol) on the Solubility of Colloidal BaTiO₃ in an Aqueous Medium. *J. Mater. Res.* 2003, 18 (5), 1266–1274.
- (35) Neige, E.; Schwab, T.; Musso, M.; Berger, T.; Bourret, G. R.; Diwald, O. Charge Separation in BaTiO₃ Nanocrystals: Spontaneous Polarization Versus Point Defect Chemistry. *Small* 2023, 19 (16), No. e2206805.
- (36) Douglass, I.; Harrowell, P. Kinetics of Dissolution of an Amorphous Solid. *J. Phys. Chem. B* 2018, 122 (8), 2425–2433.
- (37) Zu, H.; Fu, Q.; Cao, G.; Liu, H.; Huang, H.; Yan, L.; He, X.; Wang, C. Abnormal Grain Growth and Electrical Properties of Ba-Excessive La-Doped BaTiO₃ Ceramics Prepared From Nanopowder Synthesized by Sol-Gel Method. *J. Sol. -Gel. Sci. Technol.* 2023, 106 (1), 114–120.
- (38) Harris, D. T.; Burch, M. J.; Li, J.; Dickey, E. C.; Maria, J.-P. Low-Temperature Control of Twins and Abnormal Grain Growth in BaTiO₃. *J. Am. Ceram. Soc.* 2015, 98 (8), 2381–2387.
- (39) Chen, Z.; Peng, F. Normal and Abnormal Grain Growths in BaTiO₃ Fibers. *J. Am. Ceram. Soc.* 2014, 97 (9), 2755–2761.

- (40) Yuh, J.; Perez, L.; Sigmund, W. M.; Nino, J. C. Electrospinning of Complex Oxide Nanofibers. *Phys. E: Low-Dimens. Syst. Nanostruct.* **2007**, *37* (1–2), 254–259.
- (41) Bäurer, M.; Shih, S.-J.; Bishop, C.; Harmer, M. P.; Cockayne, D.; Hoffmann, M. J. Abnormal Grain Growth in Undoped Strontium and Barium Titanate. *Acta Mater.* **2010**, *58* (1), 290–300.
- (42) Chen, Y.-H.; Lu, S.-C.; Tuan, W.-H.; Chen, C.-Y. Microstructure Transition From Normal to Abnormal Grains for BaTiO₃. *J. Eur. Ceram. Soc.* **2009**, *29* (15), 3243–3248.
- (43) Yoon, B.-K.; Chin, E.-Y.; Kang, S.-J. L. Dedensification During Sintering of BaTiO₃ Caused by the Decomposition of Residual BaCO₃. *J. Am. Ceram. Soc.* **2008**, *91* (12), 4121–4124.
- (44) Adair, J. H.; Crampo, J.; Mandanas, M. M.; Suvaci, E. The Role of Material Chemistry in Processing BaTiO₃ in Aqueous Suspensions. *J. Am. Ceram. Soc.* **2006**, *89* (6), 1853–1860.